



***Ab initio* Boltzmann approach to coupled magnon-phonon thermal transport in ferromagnetic crystals**

Hui Pan , Zhong-Ke Ding, Bo-Wen Zeng, Nan-Nan Luo, Jiang Zeng, Li-Ming Tang, and Ke-Qiu Chen ^{*}
Department of Applied Physics, School of Physics and Electronics, Hunan University, Changsha 410082, China



(Received 17 December 2022; revised 13 February 2023; accepted 6 March 2023; published 15 March 2023)

We propose an *ab initio* Boltzmann transport approach taking into account magnon-phonon scattering (MPS) and three-phonon scattering simultaneously to accurately evaluate the thermal transport properties of ferromagnetic crystals. Using this approach, we studied the nonelectronic thermal transport properties of the body-centered cubic iron as a case. The reasonable agreement between our calculation results and the available experimental data suggests that phonons dominate the nonelectronic thermal conduction at high temperatures, and magnons may contribute to the thermal conductivity only at low temperatures. Remarkably, the abnormal increase in the magnon thermal conductivity at high temperatures implies that other magnon-involved scattering events instead of MPS should dominate the magnon thermal conductivity. Moreover, analyses of average scattering rates and heat propagation lengths suggest that hydrodynamic heat transport may occur at low temperatures. This new approach fills the gap in the first-principles evaluation of the coupled magnon-phonon thermal transport properties in magnetic crystals. Our results will provide valuable references for further investigations of the interplay between magnons and phonons and broaden relevant research prospects about heat management and energy manipulation.

DOI: [10.1103/PhysRevB.107.104303](https://doi.org/10.1103/PhysRevB.107.104303)

I. INTRODUCTION

Thermal transport in magnetic systems has received widespread attention with the rapid progress of spintronics [1,2] and spin caloritronics [3–5] in recent decades. A series of emerging and exciting transport phenomena governed by the interplay between spins and phonons, such as the thermal Hall effect [6–8], spin Seebeck and spin Peltier effects [9,10], and magnetocaloric effect [11], have vastly broadened the scopes of heat management and thermal manipulation and potentially inspired applications in thermoelectrics [12–14] and thermal logic gates [15,16]. However, past investigations about heat transfer were mainly devoted to nonmagnetic materials in which phonons, electrons, and the interplay between them dominate the thermal transport properties [17–20]. In contrast, the relevant studies about heat transport behavior and the interplay between magnons and phonons in magnetic systems are comparatively lacking.

In early studies, experimental measurements were mainly carried out on the thermal conductivity of magnons to detect spin quantum states [21,22] and evaluate magnon-phonon damping [23] in magnetic crystals, where the external magnetic field was usually utilized to extract the magnon's thermal conductivity. Several recent investigations focused on magnon's thermal transport properties [24–26] and magnon-phonon relaxation [27–29] in magnetic crystals. These studies suggested that magnon-phonon scattering (MPS) is crucial in explaining magnetic crystal's heat and spin transport behaviors. Consequently, mode-level insights into the MPS events

and the coupled magnon-phonon thermal transport in magnetic crystals are essential for both fundamental science and practical applications.

An *ab initio* approach urgently needs to be developed to accurately evaluate the thermal transport properties of magnetic crystals *at the mode level*. Over the past two decades, many theoretical frameworks and *ab initio* methods have been developed to evaluate the nonmagnetic materials' phonon and electron transport properties. Specifically, these methods can be broadly divided into three categories: (i) the full quantum mechanical frameworks based on the nonequilibrium Green's function (NEGF) for capturing the quantum transmission behavior of phonons and electrons in nanoscale tunneling junctions with phonon anharmonicity [30–36] or electron-phonon coupling [37–40]; (ii) the semiclassical Boltzmann transport equation (BTE) for predicting the phonon (PBTE) [41–45] and the coupled electron-phonon [46–51] transport properties of bulk materials or micro devices; (iii) the classical [52–55] or *ab initio* [56–58] molecular dynamics (MD) for statistically evaluating the thermal transport properties of large-scale systems with thousands of atoms. These methods have covered the phonon and electron transport properties in the nonmagnetic systems from quantum dots to bulk materials but rarely involved the magnon-related transport behaviors and scattering events like MPS.

Fruitful efforts have recently been made in the theoretical modeling and the numerical simulation of the thermal transport properties in magnetic systems [59]. Using the theoretical framework of the NEGF, several recent studies focused on quantum mechanical modeling of the inelastic heat or spin transfer behaviors across one-dimensional model junctions [60–63] and three-dimensional practical interfaces [64]. These

^{*}keqiuchen@hnu.edu.cn

works suggested the possibility of tuning heat transport behavior through the interplay between magnons and phonons. However, the NEGF-based methods incur high numerical computation costs and, therefore, usually are applied to small-enough (0.1–10 nm) nanodevices, which dramatically limits its scope of applications. At the same time, methods based on spin-lattice dynamics (SLD) [65–67], an extension of MD, have been developed to assess the thermal transport properties of vibrations and spins statistically in magnetic systems, such as the body-centered cubic (bcc) iron [68,69] and the Co/Cu interface [70]. One great advantage of this approach is that it can capture the thermodynamic behavior near the phase transition temperature. Still, the accuracy of the adopted potential function and the validity of this approach in small systems with strong quantum effects needs further verification. In addition, several recent studies have been devoted to modeling the spin Seebeck and spin Peltier effects [71,72], the magnetocaloric effect [73], and the magnon-phonon relaxation [74] in magnetic insulators and metals, utilizing the continuous BTE governed by magnon-phonon interaction. These studies provided no complete mode-level information about phonons and magnons with first-principles accuracy, such as magnon-phonon scattering rates and modal mean free path. However, these modal quantities are essential for a deeper understanding of the interplay between magnons and phonons and the coupled spin and heat transport behaviors.

In this paper, an *ab initio* approach (MP-BTE) coupling magnons with phonons is reported based on the theoretical framework of the Boltzmann transport equation to accurately evaluate the thermal transport properties of magnetic crystals *at the mode level*. Both magnon-phonon scattering and three-phonon scattering are incorporated into the MP-BTE to assess the scattering rates of magnons and phonons accounting for the coupled magnon-phonon thermal transport behavior. Utilizing this new approach, we studied the nonelectronic thermal transport properties of the ferromagnetic bcc iron over a broad temperature range. A reasonable agreement between our numerical results and the available experimental data is obtained. Despite the same scaling law of the calculated magnon-phonon scattering rate as that reported in previous studies [68,75], the abnormal magnon thermal conductivity at high temperatures indicates that other magnon-involved scattering events should dominate the magnon scattering. Besides, we show that a “strong-enough” magnetic field is not always able to accurately recover the magnon’s thermal conductivity from the total due to magnon-phonon scattering. Finally, the average scattering rate analysis implies that hydrodynamic heat transport phenomena may appear at low temperatures. These results would provide valuable references for further exploring the nonelectronic thermal transport in bcc iron and other magnetic materials.

This paper is organized as follows. First, the theoretical framework of the presented MP-BTE is formulated in Sec. II, and some momentous expressions and equations about the magnon-phonon scattering and the linearization of the MP-BTE are derived. To demonstrate the validity and usefulness of this method, in Sec. III, the bcc iron crystal’s coupled magnon-phonon thermal transport properties are analyzed in detail and compared with the available experimental and theoretical data. Next, in Sec. IV, we discuss the advantages and

limitations of the presented MP-BTE approach and suggest some application prospects of this method for further investigation. Finally, we conclude this study in Sec. V.

II. THEORY AND METHOD

In ferromagnetic crystals, the nonelectronic thermal transport is dominated by phonons and magnons. In the steady state, the microscopic transition rate in the distribution of phonons is governed by the steady-state BTE formulated by Peierls [76]:

$$\left. \frac{\partial n_{\mathbf{q},\lambda}}{\partial t} \right|_{\text{scat}} + \left. \frac{\partial n_{\mathbf{q},\lambda}}{\partial t} \right|_{\text{diff}} = 0, \quad (1)$$

where \mathbf{q} and λ denote the phonon’s wave vector and branch index, respectively. $n_{\mathbf{q},\lambda}$ is the undetermined phonon distribution in the steady state. The first term of the left-hand side of Eq. (1) (labeled “scat”) is the dissipation rate of phonon by internal scattering events, i.e., phonon isotope scattering, three-phonon scattering, etc. The second term (labeled “diff”) describes the phonon diffusion induced by the applied temperature gradient. Following the idea of Eq. (1), we can also write down the BTE of magnon as

$$\left. \frac{\partial n_{\mathbf{k},\gamma}}{\partial t} \right|_{\text{scat}} + \left. \frac{\partial n_{\mathbf{k},\gamma}}{\partial t} \right|_{\text{diff}} = 0, \quad (2)$$

where \mathbf{k} and γ denote the magnon’s wave vector and branch index, $n_{\mathbf{k},\gamma}$ is the steady-state distribution of magnon.

To solve the BTEs of phonon and magnon, i.e., Eqs. (1) and (2), we follow the idea of the widely used linearization approximation [77,78]. For the diffusion term, generally, the phonon (or magnon) diffusion rate driven by a small temperature gradient, namely ∇T , can be given by

$$\left. \frac{\partial n_{\ell}}{\partial t} \right|_{\text{diff}} = -\mathbf{v}_{\ell} \cdot \nabla T \frac{d\bar{n}_{\ell}}{dT}, \quad (3)$$

where ℓ denotes (\mathbf{q}, λ) or (\mathbf{k}, γ) for phonon or magnon, respectively. \mathbf{v}_{ℓ} means group velocity, and $\bar{n}_{\ell} = \bar{n}(\varepsilon_{\ell})$ is the equilibrium population, obeying Bose-Einstein statistics, of the phonon (or magnon) with energy ε_{ℓ} .

On the other hand, the scattering terms in Eqs. (1) and (2) are determined by microscopic scattering events, as shown in Fig. 1. In the presented MP-BTE method, the phonon-involved scattering processes include three-phonon scattering (\mathcal{S}_{3-p}), isotope scattering (\mathcal{S}_{p-i}), boundary scattering (\mathcal{S}_{p-b}), and magnon-phonon scattering (\mathcal{S}_{m-p}). The magnon-involved scattering processes include magnon-phonon scattering and magnon boundary scattering (\mathcal{S}_{m-b}). Notably, the first three processes involving phonons, i.e., \mathcal{S}_{3-p} , \mathcal{S}_{p-i} , and \mathcal{S}_{p-b} , have been generally considered in previous phonon transport studies based on BTE [41–45]. One can find the detailed expressions of corresponding scattering rates of these processes, respectively denoted by $\Gamma_{\lambda,\lambda',\lambda''}^{p,\pm}$, $\Gamma_{\lambda,\lambda'}^p$, and Γ_{λ}^p , in Appendix A. Here we focus on the magnon-phonon scattering process, i.e., \mathcal{S}_{m-p} .

Similarly to the case of electron-phonon scattering [79], the phonon and magnon scattering rates arising from

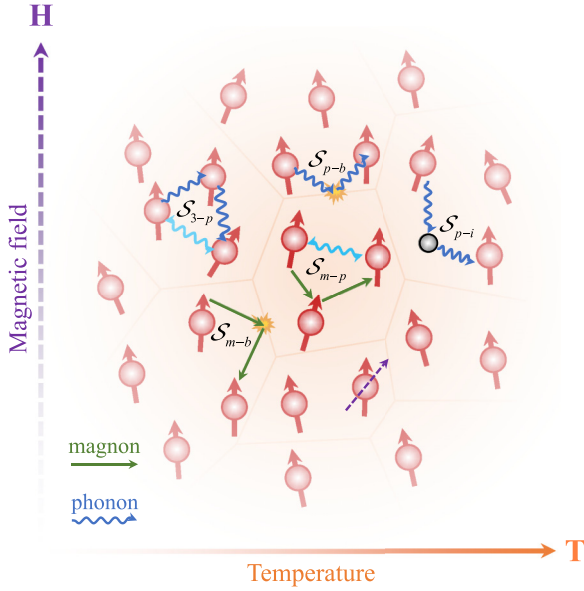


FIG. 1. Schematic of scattering processes included in the presented MP-BTE method. These magnon-involved (green straight arrow) and phonon-involved (blue wavy line with arrow) scattering processes include three-phonon scattering (S_{3-p}), phonon isotope scattering (S_{p-i}), phonon boundary (S_{p-b}) and magnon boundary (S_{m-b}) scattering, and magnon-phonon scattering (S_{m-p}). The wavy lines with double arrows indicate phonon-absorbed and phonon-emitted processes. The first three processes are generally considered in the widely used PBTE method.

magnon-phonon scattering processes have the forms

$$\Gamma_{\gamma,\gamma',\lambda}^{p,+}(\mathbf{k}, \mathbf{q}) = \frac{\pi}{\hbar} |\mathbb{M}_{\gamma,\gamma',\lambda}(\mathbf{k}, \mathbf{q})|^2 \delta(\omega_{\mathbf{q},\lambda} + \varepsilon_{\mathbf{k}-\mathbf{q},\gamma'} - \varepsilon_{\mathbf{k},\gamma}) \times (\bar{n}_{\mathbf{k}-\mathbf{q},\gamma'} - \bar{n}_{\mathbf{k},\gamma}), \quad (4)$$

$$\Gamma_{\gamma,\gamma',\lambda}^{m,\pm}(\mathbf{k}, \mathbf{q}) = \frac{\pi}{\hbar} |\mathbb{M}_{\gamma,\gamma',\lambda}(\mathbf{k}, \mathbf{q})|^2 \delta(\varepsilon_{\mathbf{k},\gamma} \pm \omega_{\mp\mathbf{q},\lambda} - \varepsilon_{\mathbf{k}-\mathbf{q},\gamma'}) \times \left(\bar{n}_{\mp\mathbf{q},\lambda} \mp \bar{n}_{\mathbf{k}-\mathbf{q},\gamma'} + \frac{1}{2} \mp \frac{1}{2} \right), \quad (5)$$

with $\delta(\varepsilon)$ the Dirac delta function. Here ε and ω denote energies of magnon and phonon, respectively. $\mathbb{M}_{\gamma,\gamma',\lambda}$ is the magnon-phonon scattering amplitude and can be obtained from the magnon-phonon coupling term of Hamiltonian as detailed in Appendix A. $\Gamma_{\gamma,\gamma',\lambda}^{p,+}$ is the phonon-magnon scattering rate corresponding to the absorption process where one phonon absorbs one magnon and turns into another magnon ($\omega_{\mathbf{q},\lambda} + \varepsilon_{\mathbf{k}-\mathbf{q},\gamma'} = \varepsilon_{\mathbf{k}+\mathbf{G},\gamma}$, \mathbf{G} denotes a reciprocal lattice vector), keeping the energy and quasimomentum conservation. $\Gamma_{\gamma,\gamma',\lambda}^{m,\pm}$ are magnon-phonon scattering rates corresponding to absorption and emission processes where one magnon absorbs or emits one phonon and turns into another magnon ($\varepsilon_{\mathbf{k},\gamma} \pm \omega_{\mathbf{q},\lambda} = \varepsilon_{\mathbf{k}\pm\mathbf{q}+\mathbf{G},\gamma'}$). All the above scattering rates were computed using data from the first-principles calculations, as discussed in Sec. III A, with the locally adaptive Gaussian approximation for the delta function [42].

According to Eq. (3), the actual distribution n_ℓ can be linearized as $n_\ell = \bar{n}_\ell - \tau_\ell^0(\mathbf{v}_\ell + \Delta_\ell) \cdot \nabla T \frac{d\bar{n}_\ell}{dT}$ with the equilibrium relaxation time τ_ℓ^0 computed as

$$\frac{1}{\tau_{\mathbf{q},\lambda}^0} = \sum_{\mathbf{q}',\lambda',\lambda''} [\Gamma_{\lambda,\lambda',\lambda''}^{p,+}(\mathbf{q}, \mathbf{q}') + \Gamma_{\lambda,\lambda',\lambda''}^{p,-}(\mathbf{q}, \mathbf{q}')] + \sum_{\mathbf{k},\gamma,\gamma'} \Gamma_{\gamma,\gamma',\lambda}^{p,+}(\mathbf{k}, \mathbf{q}) + \sum_{\mathbf{q}',\lambda'} \Gamma_{\lambda,\lambda'}^p(\mathbf{q}, \mathbf{q}') + \Gamma_{\lambda}^p(\mathbf{q}), \quad (6)$$

$$\frac{1}{\tau_{\mathbf{k},\gamma}^0} = \sum_{\mathbf{q},\gamma',\lambda} [\Gamma_{\gamma,\gamma',\lambda}^{m,+}(\mathbf{k}, \mathbf{q}) + \Gamma_{\gamma,\gamma',\lambda}^{m,-}(\mathbf{k}, \mathbf{q})] + \Gamma_{\gamma}^m(\mathbf{k}). \quad (7)$$

Here Δ_ℓ is a correction term that carries the nonequilibrium information beyond the relaxation time approximation (RTA) [80]. Γ_{λ}^p and Γ_{γ}^m are boundary scattering rates with the generalized form

$$\Gamma_{\ell}^{p(m)} = \frac{1}{L_{\text{Cas}}} |\mathbf{v}_{\ell}^{p(m)}|, \quad (8)$$

where L_{Cas} denotes the effective sample size, namely Casimir length, dependent on the geometry of the grain boundary [81,82]. In this way, the resulting linearized BTE can be concisely written as [43,78]

$$\mathbf{F}_\ell = \tau_\ell^0(\mathbf{v}_\ell + \Delta_\ell). \quad (9)$$

The expression of the correction term, including only three- and two-phonon scattering processes, has been given in the PBTE method [78,83]. However, unlike the case in PBTE, the correction term Δ_ℓ in the presented MP-BTE is composed of two parts, i.e., phonon and magnon parts, respectively denoted by $\Delta_{\mathbf{q},\lambda}$ and $\Delta_{\mathbf{k},\gamma}$. Considering all the scattering processes shown in Fig. 1, these two correction terms have forms

$$\begin{aligned} \Delta_{\mathbf{q},\lambda} = & \sum_{\mathbf{q}',\lambda',\lambda''} \Gamma_{\lambda,\lambda',\lambda''}^{p,+}(\mathbf{q}, \mathbf{q}') (\xi_{\mathbf{q},\lambda}^{\mathbf{q}',\lambda''} \mathbf{F}_{\mathbf{q}',\lambda''}^p - \xi_{\mathbf{q},\lambda}^{\mathbf{q}-\mathbf{q},\lambda'} \mathbf{F}_{\mathbf{q}-\mathbf{q},\lambda'}^p) \\ & + \sum_{\mathbf{q}',\lambda',\lambda''} \Gamma_{\lambda,\lambda',\lambda''}^{p,-}(\mathbf{q}, \mathbf{q}') (\xi_{\mathbf{q},\lambda}^{\mathbf{q}',\lambda''} \mathbf{F}_{\mathbf{q}',\lambda''}^p + \xi_{\mathbf{q},\lambda}^{\mathbf{q}-\mathbf{q},\lambda'} \mathbf{F}_{\mathbf{q}-\mathbf{q},\lambda'}^p) \\ & + \sum_{\mathbf{k},\gamma,\gamma'} \Gamma_{\gamma,\gamma',\lambda}^{p,+}(\mathbf{k}, \mathbf{q}) (\xi_{\mathbf{q},\lambda}^{\mathbf{k},\gamma} \mathbf{F}_{\mathbf{k},\gamma}^m - \xi_{\mathbf{q},\lambda}^{\mathbf{k}-\mathbf{q},\gamma'} \mathbf{F}_{\mathbf{k}-\mathbf{q},\gamma'}^m) \\ & + \sum_{\mathbf{q}',\lambda'} \Gamma_{\lambda,\lambda'}^p(\mathbf{q}, \mathbf{q}') \xi_{\mathbf{q},\lambda}^{\mathbf{q}',\lambda'} \mathbf{F}_{\mathbf{q}',\lambda'}^p, \end{aligned} \quad (10)$$

$$\begin{aligned} \Delta_{\mathbf{k},\gamma} = & \sum_{\mathbf{q},\gamma',\lambda} \Gamma_{\gamma,\gamma',\lambda}^{m,-}(\mathbf{k}, \mathbf{q}) (\xi_{\mathbf{k},\gamma}^{\mathbf{q},\lambda} \mathbf{F}_{\mathbf{q},\lambda}^p + \xi_{\mathbf{k},\gamma}^{\mathbf{k}-\mathbf{q},\gamma'} \mathbf{F}_{\mathbf{k}-\mathbf{q},\gamma'}^m) \\ & + \sum_{\mathbf{q},\gamma',\lambda} \Gamma_{\gamma,\gamma',\lambda}^{m,+}(\mathbf{k}, \mathbf{q}) (\xi_{\mathbf{k},\gamma}^{\mathbf{k}-\mathbf{q},\gamma'} \mathbf{F}_{\mathbf{k}-\mathbf{q},\gamma'}^m - \xi_{\mathbf{k},\gamma}^{\mathbf{q},\lambda} \mathbf{F}_{\mathbf{q},\lambda}^p), \end{aligned} \quad (11)$$

with the shorthand symbol $\xi_{\ell}^{\ell} = \varepsilon_\ell / \varepsilon_{\ell'}$, where $\Gamma_{\lambda,\lambda',\lambda''}^{p,\pm}$ are three-phonon scattering rates corresponding to absorption and emission processes.

Note that $\Delta_{\mathbf{q},\lambda}$ and $\Delta_{\mathbf{k},\gamma}$ are interrelated through \mathbf{F}_ℓ and thus cannot be determined separately. Several numerical algorithms, namely iteration method [78,84], direct method [44,83], and variational method [43], have been suggested to

solve this set of self-consistent equations, i.e., Eqs. (9)–(11). In this work, we adopt the direct method to obtain the exact solution of MP-BTE. The final thermal conductivity can be yielded in terms of \mathbf{F}_ℓ as

$$\kappa_x^{\alpha,\beta} = \frac{1}{k_B T^2 \Omega N} \sum_\ell \varepsilon_\ell^2 \bar{n}_\ell (\bar{n}_\ell + 1) v_\ell^\alpha F_\ell^\beta, \quad (12)$$

where x labels phonon (p) or magnon (m). k_B , Ω , and N are the Boltzmann constant, the unit cell's volume, and the sampling number of \mathbf{k} (or \mathbf{q}) grid points, respectively. This expression can also be written as $\kappa_x^{\alpha,\beta} = \sum_\ell C_\ell v_\ell^\alpha F_\ell^\beta$ with C_ℓ the heat capacity of the mode ℓ . Incidentally, when $\Delta_\ell = 0$, Eq. (12) will degenerate into the version under the RTA.

III. VALIDATION AND RESULTS

In this section, we apply the above MP-BTE method to the natural isotopic bcc iron with ferromagnetic order to verify the validity of this approach and investigate relevant thermal transport properties. First, in Sec. III A, the dispersion relations of magnon and phonon, obtained from first-principles calculations, are compared with available experimental data to demonstrate the accuracy of the parameters used in this work. The computational details are illustrated incidentally. Next, the thermal conductivities of magnon and phonon are calculated at the temperature range from 10 K to 1000 K, in Sec. III B, and compared with the available experimental and theoretical results. Furthermore, in Sec. III C, we analyze the influence of magnon-phonon scattering on the heat conductance of magnon and phonon at the mode level in detail. After that, in Sec. III D, the thermal transport behavior tuned by an external magnetic field is also further explored at various temperatures. Finally, the possibility of hydrodynamic heat transport in the present bcc iron is indicated in Sec. III E.

A. Dispersion relations and computational details

The accurate calculation of magnon and phonon energy spectra is crucial in searching for scattering processes that satisfy both energy and momentum conservation. We computed the dispersion relations of phonons (solid blue line, left axis) and magnons (solid red line, right axis), as plotted in Fig. 2, utilizing first-principles calculations based on the density functional theory (DFT). As a comparison, the available neutron-scattering data of phonon (square marker) and magnon (circle marker) spectra are also given. The calculated results are considerably consistent with the experimental data, confirming the input parameters from our first-principles calculations are reliable.

The spin-polarized DFT calculation was implemented in the Vienna *ab initio* simulation package (VASP) [87,88] within the projector augmented-wave method [89,90] using the generalized gradient approximation (GGA) and Perdew-Burke-Ernzerhof exchange-correlation functional (PBE) [91]. An energy cutoff of 500 eV was used, and a convergence threshold of 10^{-8} eV was adopted for each self-consistent electronic step. First, a relaxation process of the primitive cell of bcc iron ran with a k mesh of $16 \times 16 \times 16$ until the maximum force was smaller than 10^{-4} eV/Å² on each atom. After that, all input parameters of the

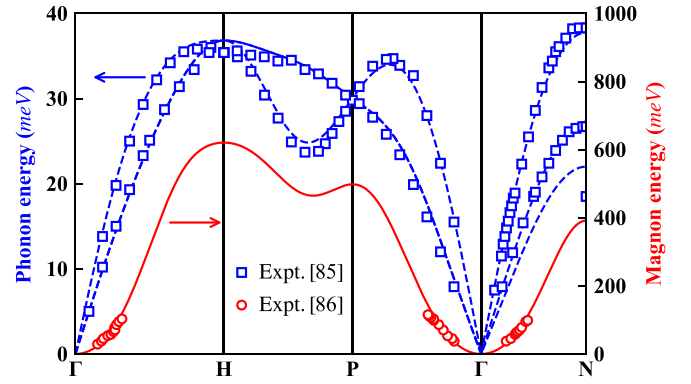


FIG. 2. First-principles phonon (dashed blue line, left axis) and magnon (solid red line, right axis) spectrum of ferromagnetic bcc iron. The results are compared with available neutron-scattering data of phonon (square marker, from Ref. [85]) and magnon (circle marker, from Ref. [86]) spectra, respectively.

MP-BTE method, i.e., exchange-coupling constants (ECCs), second-order force constants (2nd-IFCs), third-order force constants (3rd-IFCs), and *exchange-force constants* (the linear expansion coefficient of ECCs to the displacement of the atom, denoted by EFCs) (see Appendix A for the definition), were computed on a $4 \times 4 \times 4$ supercell of the optimized cell.

The Hellmann-Feynman force was computed in VASP using a k mesh of $4 \times 4 \times 4$ for evaluating 2nd-IFCs and 3rd-IFCs. The 2nd-IFCs were computed by the PHONOPY package [92] combined with density functional perturbation theory implemented in VASP. The crystal symmetry and acoustic sum rule [93] were applied to ensure the obtained 2nd-IFCs are physical. The 3rd-IFCs were calculated by the thirdorder.py code [78] with a cutoff radius to the seventh nearest-neighbor atom (about 0.7 nm), which is enough to obtain accurate three-phonon scattering information [69]. On the other hand, to evaluate the magnetism-related parameters, i.e., ECCs and EFCs, the spin-polarized DFT calculation was performed in the OpenMX code [94,95] using GGA+PBE schema with an energy cutoff of 600 Ry and a convergence criterion of 10^{-8} Hartree. The ECCs were computed based on the Liechtenstein method [96,97] implemented in our in-house code interfaced with the OpenMX code. A larger k mesh of $7 \times 7 \times 7$ was adopted here to ensure these magnetism-related parameters, i.e., ECCs and EFCs, were evaluated accurately. The EFCs were obtained from the finite displacement method, as detailed in Appendix A. In our calculations, the magnetic moments of Fe atoms in bcc iron are about $2.216 \mu_B$, and the nearest-neighbor ECC is about 21.4 meV (the corresponding Curie temperature is about 1326 K), basically agreeing with previous studies [98,99].

After the above calculations, we obtained all the input data for MP-BTE, i.e., 2nd-IFCs, 3rd-IFCs, ECCs, and EFCs. In this method, the energy spectrum of the magnon was determined by the magnon's dynamical matrices formulated by the ECCs, and phonon energies were obtained by diagonalizing the phonon's dynamical matrices computed by the 2nd-IFCs. The scattering amplitudes of three-phonon scattering ($\mathbb{V}_{\lambda,\lambda',\lambda''}$) and magnon-phonon scattering ($\mathbb{M}_{\gamma,\gamma',\lambda}$) were computed from 3rd-IFCs and EFCs, respectively. The specific expressions

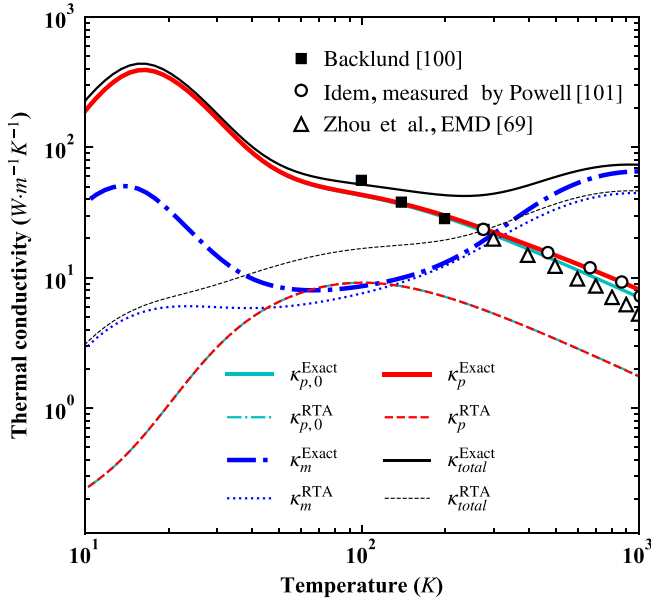


FIG. 3. Temperature dependence of phonon (κ_p^X , solid or dashed red line), magnon (κ_m^X , dash-dotted or dotted blue line), and total (κ_{total}^X , dark solid or dashed line) thermal conductivities from exact solution (κ_{exact}^X) or RTA (κ_{RTA}^X) of MP-BTE with the Casimir length of 100 μm . As a comparison, the temperature-dependent phonon thermal conductivity without MPS ($\kappa_{p,0}^X$, solid or dash-dotted cyan line) is plotted. The results are compared with available experimental (square and circle symbols) and computational (triangle symbols) data of nonelectronic thermal conductivity from Refs. [69,100,101].

for transforming these real-space matrices to the reciprocal versions can be found in Appendix A. A k mesh of $28 \times 28 \times 28$ was adopted in the MP-BTE calculation to obtain convergent thermal conductivities for both magnon and phonon (see Appendix B for the convergence test). It should be noted that, unlike the spin-lattice coupling, the magnon-phonon scattering mainly focuses on the energy exchange between the spin waves and the atomic vibrations. The static part of exchange-coupling-induced phonon renormalization had been contained in the spin-polarized calculations of IFCs [64].

B. Nonelectronic thermal conductivity

Taking into account the magnon-phonon scattering, the exact solutions of phonon thermal conductivities (κ_p^{Exact}) agree well with the experimental measurements (nonelectronic thermal conductivity) in high-purity iron samples with a grain boundary size of about 100 μm [100,101] (unless otherwise specified, this boundary size would be used in all calculations below), at temperatures above 200 K (see the circles in Fig. 3). However, when the temperature drops to 100 K, the exact solution of the total thermal conductivity ($\kappa_{\text{total}}^{\text{Exact}} = \kappa_p^{\text{Exact}} + \kappa_m^{\text{Exact}}$) instead of the phonon thermal conductivity is consistent well with the experimental data (see squares in Fig. 3). Specifically, magnons make a remarkable contribution of about 17% to the total thermal conductivity at the temperature of 100 K. The above results suggest phonons instead of magnons dominate the nonelectronic thermal transport at high temperatures (above 200 K). Nonetheless, the contribution of

magnons to the nonelectronic thermal conductivity needs to be attracted to attention at low temperatures (below 100 K).

Furthermore, it is also noted that the experimental results and $\kappa_{\text{total}}^{\text{Exact}}$ have opposite trends due to the anomalous raising of κ_m^{Exact} over the temperature range from 200 K to 1000 K, as shown in Fig. 3. Although this trend may be reasonable since the Curie temperature of the bcc iron is up to 1300 K (see Appendix D for qualitative analyses). However, in this temperature region, the predicted thermal conduction of magnons is dominated by magnon-phonon scattering processes. These unrealistically high thermal conductivities of magnons indicate that other kinds of scattering events, such as magnon-magnon and magnon-impurity scattering, should be further considered to suppress the magnon heat conduction at temperatures above 200 K.

Besides, temperature-induced lattice expansion and spin disorder may also be necessary for reasonable nonelectronic thermal conductivity at high temperatures [102]. As a comparison, the nonelectronic thermal conductivities from a previous study based on the equilibrium molecular dynamics [69] are also plotted (triangle symbols) in Fig. 3, which is in broad agreement with experimental measurements. This work also suggested that the MPS contributes little to the total thermal conductivity at high temperatures above 300 K, agreeing with our prediction. Due to the inhomogeneity of practical iron samples, nevertheless, we do not intend to address this issue here and only focus on the introduction of MPS and its influence on magnons and phonons.

C. Influence of the MPS on phonons and magnons

To further illustrate the role of the MPS in thermal transport, this section analyzes the influences of the MPS on phonon and magnon at the mode level.

First, the phonon scattering rates induced by the MPS (red circle symbols, τ_{p-m}^{-1}) and all other phonon-involved processes (black square symbols, $\tau_{p-p}^{-1} + \tau_{p-b}^{-1}$) at temperatures of 100, 300, and 1000 K are shown in Fig. 4. It is seen that the phonon scattering rates induced by the MPS are much (about two orders of magnitudes) smaller than that induced by all other scattering processes at all temperatures. Moreover, in the high-energy region (red dashed circle), the gap between these two groups of scattering rates decreases with rising temperature. These results suggest that the magnon-phonon scattering has little impact on the phonon relaxation and the phononic thermal conduction in bcc iron. This point can also be seen from the exact phonon thermal conductivities with (κ_p^{Exact}) and without MPS ($\kappa_{p,0}^{\text{Exact}}$), as shown in Fig. 3. The gap between $\kappa_{p,0}^{\text{Exact}}$ and κ_p^{Exact} increases with the temperature but is still small enough (the percentage of the gap to κ_p^{Exact} is about 4.8% at 300 K and about 12.7% at 1000 K) to be neglected.

We noticed that a recent SLD-based study [69] also suggested that introducing the MPS hardly affects the phonon thermal conductivity in bcc iron. Theoretically, this may be attributed to the slight overlap of the density of states between magnons and phonons, resulting in a magnon-phonon scattering far smaller than three-phonon scattering. A similar case may be found in electron-phonon interaction. Since the electron's energy in materials is typically far greater than the

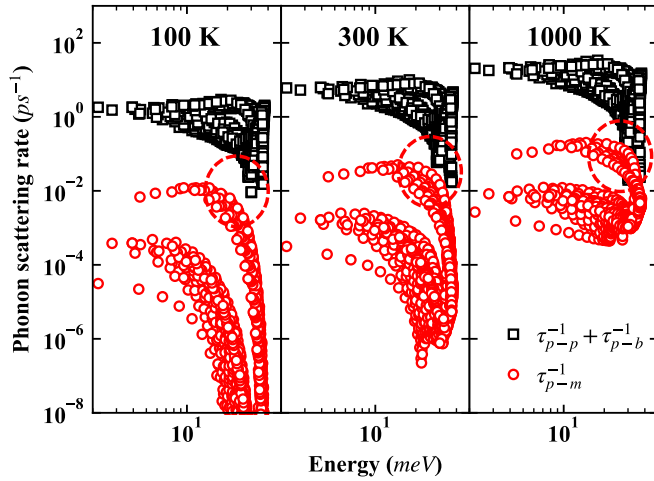


FIG. 4. Phonon scattering rates from magnon-phonon scattering processes (τ_{p-m}^{-1} , square black marker) and from all other (phonon-phonon scattering $\tau_{p-p}^{-1} = \tau_{3-p}^{-1} + \tau_{p-i}^{-1}$ and phonon boundary scattering τ_{p-b}^{-1} , circle red marker) processes at 100, 300, and 1000 K. The overlap area between τ_{p-m}^{-1} and $\tau_{p-p}^{-1} + \tau_{p-b}^{-1}$ in red dashed circle increases with temperature increasing.

phonon's, the phonon scattering induced by electron-phonon interaction can be neglected in most materials.

On the other hand, to show the influence of the MPS on magnons, as shown in Fig. 5, we plotted the scattering rate (τ_m^{-1}), exact mean free path [$\lambda_m(\varepsilon_\ell) = |\mathbf{F}_\ell|$], modal thermal conductivity ($\kappa_{m,\text{mod}}^{\text{Exact}}$), and the cumulative thermal conductivity [$\kappa_{m,\text{cum}}^{\text{Exact}}(\varepsilon_\ell) = \sum_{\ell'} \kappa_{m,\ell'}^{\text{Exact}} \theta(\varepsilon_\ell - \varepsilon_{\ell'})$, where $\theta(\varepsilon)$ is the

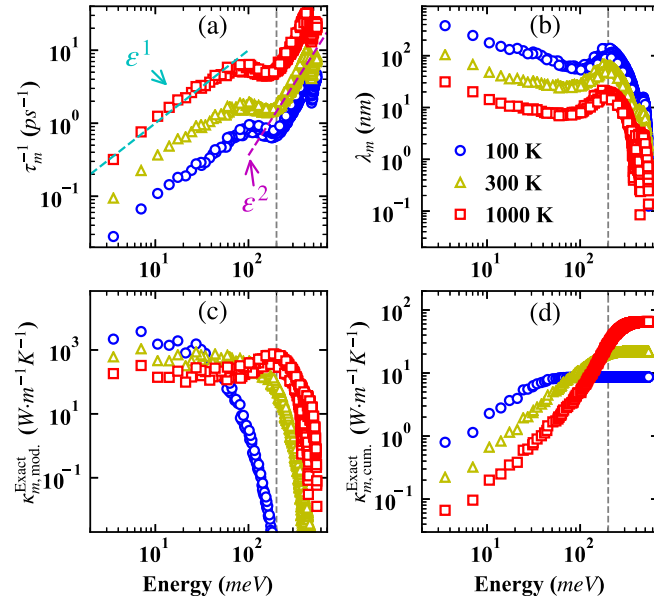


FIG. 5. Temperature dependence of magnon (a) scattering rate τ_m^{-1} , (b) exact mean free path λ_m , (c) modal thermal conductivity $\kappa_{m,\text{mod}}^{\text{Exact}}$, and (d) cumulative thermal conductivity $\kappa_{m,\text{cum}}^{\text{Exact}}$, at 100 K (circle marker), 300 K (triangle marker), and 1000 K (square marker). ε denotes the magnon's energy here. The power laws of $\tau_m^{-1} \sim \varepsilon^{-1}$ below 100 meV and $\tau_m^{-1} \sim \varepsilon^{-2}$ above 200 meV are consistent well with that suggested in Refs. [68,75].

Heaviside step function] of magnons at different temperatures. Figure 5(a) shows the total magnon scattering rates induced by the MPS and the magnon-boundary scattering with a Casimir length of 100 μm at 100, 300, and 1000 K. The magnon-boundary scattering rates are not separately shown here since they are approximately three orders more minor than the MPS-induced scattering rates. Remarkably, the magnon scattering rate varies directly as ε^{-1} below the energy of about 100 meV and directly as ε^{-2} above the energy of about 200 meV, which agrees well with previous studies [68,75,103]. Nevertheless, the magnon damping in bcc iron cannot be considered dominated by the magnon-phonon scattering since the resulting magnon thermal conductivity shown in Fig. 3 is markedly overestimated. This result indicates that other scattering events, like four-magnon scattering, may need further consideration.

To further explain the anomalous raising of magnon thermal conductivity above 100 K, we show the mean free path (λ_m) and the modal thermal conductivity (κ_m^{Exact}) of magnons in Figs. 5(b) and 5(c), respectively. It is seen that, with the temperature rising, the mean free path normally decreases, whereas the resulting thermal conductivity of magnons with energy above 100 meV increases anomalously. According to the expression of thermal conductivity in Eq. (12), the only two temperature-dependent variables governing thermal conductivity are the mean free path and the specific heat capacity. Accordingly, the abnormal increase of magnon thermal conductivity should be attributed to the sharp increases in the occupation (\bar{n}_ℓ) and the specific heat capacity of magnons with energy above 100 meV. To show this point intuitively, we plotted the magnon cumulative thermal conductivity as a function of energy in Fig. 5(d). One can observe the great contribution of magnons with energy between 100 and 200 meV to the abnormal increase in thermal conductivity. These results suggest that other kinds of scattering events, such as magnon-magnon scattering, should be of further concern because the magnon thermal conductivity is greatly overestimated at temperatures above 100 K.

D. Effect of the external magnetic field

A “strong-enough” magnetic field is usually applied in thermal measurements of magnetic materials to “freeze” low-energy magnons, extracting the magnon's contribution from the total thermal conductivity [104–106] (see also Appendix C for more details). Despite the complexity of thermal transport in the practical bcc iron, where electrons, phonons, and magnons coexist, in this section, we still show the nonelectronic thermal transport behaviors tuned by external magnetic fields at various temperatures as a reference for further study.

The nonelectronic thermal transport behaviors tuned by external magnetic field H (H here denotes the magnetic-field-induced Zeeman energy with the unit of meV) at various temperatures are shown in Fig. 6. First, as shown in Fig. 6(a), we plotted the ratio of exact thermal conductivity with the magnetic field of H to that with $H = 0$, i.e., $\kappa^{\text{Exact}}(H)/\kappa^{\text{Exact}}(0)$, for magnons, phonons, and the total as a function of H at the temperature of 10 K. Remarkably, the thermal conductivity of magnons visibly depends on the external magnetic field, while the phonon's thermal conductivity is

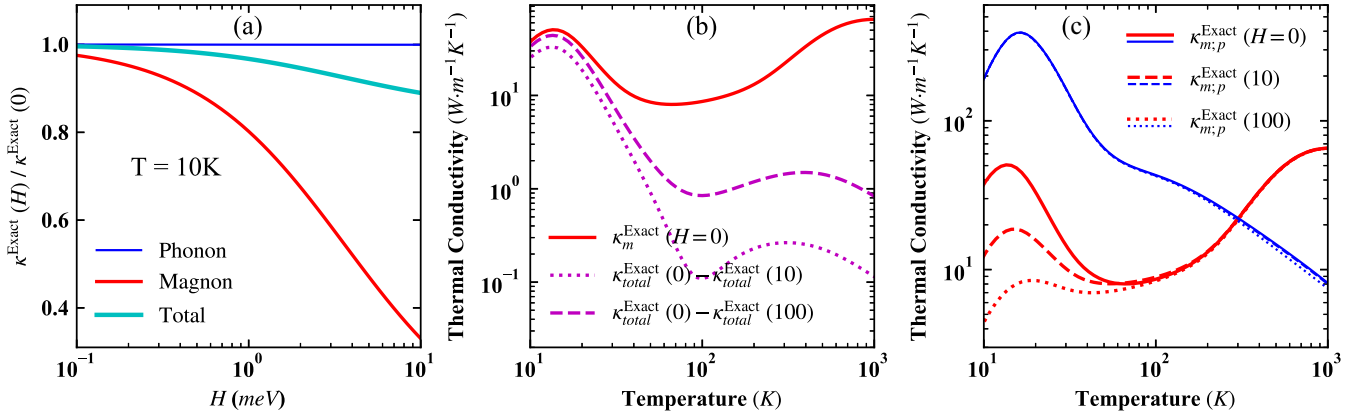


FIG. 6. Nonelectronic thermal conductivities tuned by external magnetic fields at various temperatures. (a) The ratio of the exact thermal conductivity with the magnetic field of H to that with $H = 0$ meV at the temperature of 10 K, respectively, for phonon (blue thin line), magnon (red line), and the total (cyan bold line). (b) Magnon's thermal conductivity with $H = 0$ meV (red solid line), compared with differences between the total thermal conductivity without magnetic field and that with $H = 10$ meV (red dashed line) as well as $H = 100$ meV (dotted red line). (c) The temperature dependence of exact thermal conductivities of magnons (red bold lines) and phonons (blue thin lines), with various magnetic fields of 0 meV (solid lines), 10 meV (dashed lines), and 100 meV (dotted lines).

hardly affected. The total thermal conductivity decreases by about 10% as H increases from 0 to 10 meV (equivalent to a strong magnetic induction of about 86 T). However, even if such a strong field is applied, the contribution of magnons to thermal conductivity can still not be neglected, which indicates that a stronger field or a lower temperature is required to remove the magnon's thermal conduction.

To illustrate how strong a magnetic field is required in experimental measurements to obtain an accurate magnon's thermal conductivity at various temperatures, we plotted the differences between the total thermal conductivity without an external magnetic field and that with $H = 10$ meV (dotted line) as well as $H = 100$ meV (dashed line) in Fig. 6(b). As a comparison, the exact thermal conductivity of magnons was also plotted [solid line, $\kappa_m^{\text{Exact}}(H = 0)$]. We adopted the convention $\kappa_{\text{total}}^{\text{diff}}(H) = \kappa_{\text{total}}^{\text{Exact}}(0) - \kappa_{\text{total}}^{\text{Exact}}(H)$ to simplify the description below. One can see that the stronger the magnetic field H is, the closer $\kappa_{\text{total}}^{\text{diff}}(H)$ is to $\kappa_m^{\text{Exact}}(H = 0)$. However, there are still visible relative errors of about 11% and 21% between $\kappa_m^{\text{Exact}}(H = 0)$ and $\kappa_{\text{total}}^{\text{diff}}(100)$ at temperatures 10 and 20 K, respectively. With temperature further rising, this relative error increases to about 93% and 98% at temperatures 300 and 1000 K. These results imply that a “strong-enough” magnetic field still hardly separates the magnon's thermal conductivity from the total in bcc iron at temperatures above 10 K. However, for ferromagnetic materials with high-energy magnons, the magnon's thermal conductivity should also be important at high temperature. Therefore, the coupled magnon-phonon transport theories and the relevant numerical methods thus are necessary.

It is noteworthy that in the above idea of evaluating $\kappa_m^{\text{Exact}}(H = 0)$ using $\kappa_{\text{total}}^{\text{diff}}(H)$, the assumption that the magnetic field only affects the magnons has been used. However, this assumption may not always be reasonable because magnons and phonons are coupled, and the magnetic field can also indirectly influence phonons. To illustrate this point, Fig. 6(c) shows the temperature-dependent thermal conductivity, of magnons and phonons, with various magnetic fields of 0, 10, and 100 meV. At temperatures below 100 K, the change

in the total thermal conductivity mainly originates from magnons, while phonons dominate at temperatures above 100 K. Meanwhile, remember the discussion in Sec. III C, at temperatures above 100 K, the MPS slightly enhances the phonon thermal conductivity. These results indicate that the magnon thermal conductivity (κ_m^{Exact}) may be wrongly evaluated in ferromagnets with strong MPS since the enhanced part of the phonon thermal conductivity will be regarded as a part of the κ_m^{Exact} if determining $\kappa_m^{\text{Exact}}(H = 0)$ using $\kappa_{\text{total}}^{\text{diff}}(H)$. The misestimated part of the magnon thermal conductivity is induced by the MPS and should enlarge with the enhancement of the MPS.

E. Possible hydrodynamic heat transport

Remarkably, the thermal conductivity at the RTA level is far smaller (about one order of magnitude for magnons and three orders of magnitude for phonons at 10 K) than that with the exact solution at low temperatures, which usually indicates a hydrodynamic heat transport may occur [107].

To analyze the transport state of coupled magnons and phonons under various conditions (temperature and grain size), we define the thermodynamic averages of several physical quantities as follows [108]:

$$\tau_{\text{T(N,R),av}}^{-1} = \frac{\sum_{\ell} C_{\ell} \tau_{\text{T(N,R),\ell}^0}^{-1}}{\sum_{\ell} C_{\ell}}, \quad (13)$$

$$v_{\text{av}}^2 = \frac{\sum_{\ell} C_{\ell} \mathbf{v}_{\ell} \cdot \mathbf{v}_{\ell}}{\sum_{\ell} C_{\ell}}, \quad (14)$$

$$\Lambda_{\text{av}}^{\text{RTA}} = v_{\text{av}} / \tau_{\text{T,av}}^{-1}, \quad (15)$$

where $\tau_{\text{T(N,R),av}}^{-1}$ is the average scattering rate with “N”, “R”, and “T” denoting the N-scattering process (intrinsic scattering processes with momentum conservation), the R-scattering process, i.e., intrinsic scattering processes without momentum conservation (U-scattering processes) and boundary scattering processes, and all processes (N- and R-scattering processes), respectively.

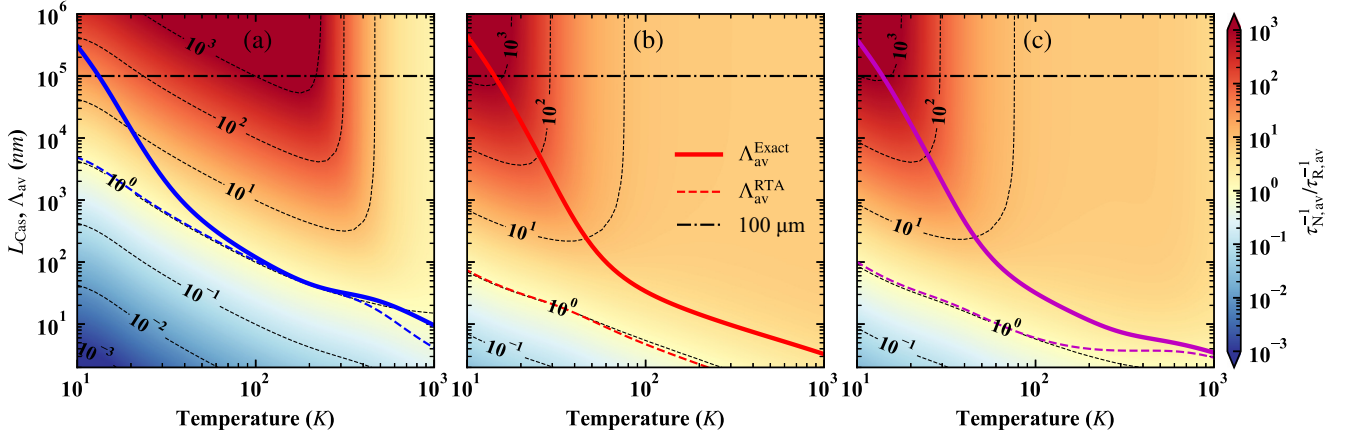


FIG. 7. The propagation length ($\Lambda_{av}^{\text{Exact}}$, solid line, using exact solution; $\Lambda_{av}^{\text{RTA}}$, dashed line, at the RTA level) of (a) magnon (blue lines), (b) phonon (red lines), and (c) the total (purple lines), as a function of the temperature. Note that (a) and (c) share the same legend (except the color of lines for propagation length) with (b). The contour maps filled with colors denote the ratio of the average scattering rate of N-processes to that of R-processes, namely $\tau_{N,av}^{-1}/\tau_{R,av}^{-1}$, for (a) magnon, (b) phonon, and (c) the total, with respect to the temperature and the Casimir length L_{Cas} . The line at 100 μm (dash-dotted black line) is plotted as a reference.

v_{av}^2 is the average square velocity. As before, C_ℓ and \mathbf{v}_ℓ are the specific heat capacity and the group velocity of magnon (or phonon) at mode ℓ , respectively. $\Lambda_{av}^{\text{RTA}}$ is the heat propagation length under RTA. For the exact solution, the heat propagation length is given by

$$\Lambda_{av}^{\text{Exact}} = v_{av}/\tau_{T,av}^{-1, \text{Exact}}, \quad (16)$$

where the average *exact* scattering rate $\tau_{T,av}^{-1, \text{Exact}}$ has the form

$$\tau_{T,av}^{-1, \text{Exact}} = \frac{\sum_\ell C_\ell \mathbf{v}_\ell \cdot \mathbf{v}_\ell}{\sum_\ell C_\ell |\mathbf{v}_\ell \cdot \mathbf{F}_\ell|}. \quad (17)$$

Note that boundary scattering is not considered while calculating the propagation lengths, meaning that the propagation lengths defined here characterize an intrinsic transport property unrelated to the grain boundary. Notably, the *exact* propagation lengths are primarily limited by the U-scattering events since the N-scattering events do not directly contribute to thermal resistance under the exact solution.

Figures 7(a)–7(c) show the heat propagation length [$\Lambda_{av}^{\text{Exact(RTA)}}$, vertical axis, without boundary scattering] and the ratio, with different Casimir lengths (L_{Cas} , vertical axis), of the average N-scattering rate to the average R-scattering rate ($\tau_{N,av}^{-1}/\tau_{R,av}^{-1}$, contour maps filled with colors) at various temperatures for magnon, phonon, and the total, respectively. It is seen that the average propagation length using exact solution ($\Lambda_{av}^{\text{Exact}}$, solid line) is far greater (two orders of magnitude for magnons, and about four orders of magnitude for phonons, at 10 K) than that with RTA ($\Lambda_{av}^{\text{RTA}}$, dashed line), which usually indicates a hydrodynamic heat transport may occur. The blue areas below the lines of $\Lambda_{av}^{\text{RTA}}$, corresponding to $\tau_{N,av}^{-1} \ll \tau_{R,av}^{-1}$, are the *ballistic* region where the boundary scattering limits the heat transport. The yellow areas above the line of $\Lambda_{av}^{\text{Exact}}$ are the *diffusive* region where the R-scattering limits the heat transport.

Following Guyer's conditions [109], two conditions need to be met to detect the hydrodynamic heat transport phenomenon: (i) $\tau_{N,av}^{-1} \gg \tau_{R,av}^{-1}$ and (ii) $L_{Cas} \lesssim \Lambda_{av}^{\text{Exact}}$. The first

condition ensures that the N-scattering dominates the heat transport so that the heat carriers collectively move with a slowly dissipated global momentum and produce the temperature wave. The second condition ensures that the temperature wave is still maintained well when reaching the probing boundary, such as the grating boundary [110]. According to the above two conditions, if the grain boundary size is selected as 100 μm (dark dash-dotted lines), then the hydrodynamic heat transport will occur at the temperature range from 10 to 14 K [the intersection of $\Lambda_{av}^{\text{Exact}}$ and the line of 100 μm in Fig. 7(c)]. In this region, the value of $\tau_{N,av}^{-1}/\tau_{R,av}^{-1}$ is between 10^1 and 10^2 for magnons and over 10^3 for phonons, suggesting both magnons and phonons may be simultaneously in the hydrodynamic regime. It shall inspire great interest in not only the phonon hydrodynamic heat transport but also the magnon hydrodynamic spin transport. However, since the bcc iron is metallic, the electrons should also play an essential role in such dynamic heat transport behaviors through electron-phonon coupling. Therefore, we can make no more conclusions about the hydrodynamic heat transport in the bcc iron but only give an inspiring reference for further studies about relevant topics.

IV. DISCUSSION

Due to the complexity of couplings among different carriers (phonons, magnons, and electrons), accurately calculating and decoupling the thermal conductivity in bcc iron is still challenging. Both the anomalous thermal conductivity of magnons at high temperatures and the possible hydrodynamic heat transport behavior at low temperatures are crucial for a deeper understanding of the coupled magnon-phonon heat transport in ferromagnetic systems like bcc iron. The MP-BTE method allows people to investigate thermal transport properties in ferromagnetic crystals *at the mode level* with first-principles accuracy and therefore is complementary to other methods such as NEGF [63,64] and SLD [67–69]. Specifically, this method fills the gap in the *ab initio* BTE

method for evaluating the heat transport properties of magnetic crystals and is expected to vastly broaden the research scope of thermal transport, combining with an array of tuning means, such as phase transition [111], stacking and twisting [112,113], gating [114], and strain [115].

Before concluding our study, we briefly highlight two limitations that our methodology inherited from the linearized Boltzmann transport equation. All these constants, i.e., ECCs, 2nd-IFCs, 3rd-IFCs, and EFCs, are computed by first-principles adiabatically, which means the effects of temperature on magnon spectrum, phonon spectrum, and magnon-phonon coupling strength are not considered. However, these effects may also be essential to heat transport properties at high temperatures, especially around the Curie temperature [69,102]. Therefore, the MP-BTE method is not appropriate for the case that is far away from the perturbation approximation. Furthermore, the linear approximation adopted in Eq. (3) requires the applied temperature gradient (∇T) to be small enough that the deviation of phonon (magnon) distribution can be expressed in terms of the linear order of ∇T . As a result, the small-size (0.1–10 nm) systems' thermal conductivities given by the MP-BTE at low temperatures (ballistic limit) may hardly reflect the practical situation quantitatively.

However, even so, the MP-BTE method can still give essential and in-depth insights into the coupled heat and spin transport behaviors in magnetic systems *at the mode level* and is expected to provide inspiring and valuable references to practical applications such as thermoelectric devices [116] and thermal logic gates [117,118].

V. CONCLUSIONS

In conclusion, we have developed an *ab initio* Boltzmann transport approach, namely MP-BTE, coupling magnon with phonon, incorporating both magnon-phonon scattering and three-phonon scattering, for the accurate evaluation of thermal transport properties in ferromagnetic materials. Remarkably, the MP-BTE method can directly decouple and analyze scattering rates induced by various scattering events *at the mode level*. The reasonable agreement between our calculation results and the available experimental and theoretical data suggests the validity of this approach in capturing the coupled heat transfer behavior of magnons and phonons in magnetic crystals. Besides, the strong magnon-phonon scattering may induce to obtain an unreliable magnon thermal conductivity in the thermal measurement under a strong magnetic field. In addition, the potential hydrodynamic behavior of magnons and phonons should attract considerable attention to the low-temperature heat conduction in magnetic crystals. However, at high temperatures, other kinds of scattering events, such as magnon-magnon and magnon-impurity scattering, should be further considered to obtain reliable information about magnon scattering. This new approach paves the way for the first-principles investigation of the coupled magnon-phonon transport behaviors in magnetic crystals *at the mode level*, thus broadening the research prospects of heat management and energy manipulation. The application of this method will provide distinctive and deeper insights into the interplay between magnons and phonons in other magnetic materials.

ACKNOWLEDGMENTS

This work was financially supported by the National Key Research and Development Program of Ministry of Science and Technology (2022YFA1402504) and by the National Natural Science Foundation of China (Grants No. 11974106 and No. 12004106). Numerical computations were performed at the National Supercomputer Center in Changsha.

APPENDIX A: MATRIX TRANSFORMATION AND SCATTERING AMPLITUDES

This section shows the transformation expressions of some matrices used in the main text and derives the scattering amplitudes of three-phonon scattering and magnon-phonon scattering.

The energy spectra of magnons and phonons are obtained by respectively diagonalizing the magnon's and phonon's dynamic matrices [64]:

$$\mathcal{X}_{i,j}(\mathbf{k}) = \frac{1}{\sqrt{S_i S_j}} \sum_m X_{i,j}(m, 0) \exp[-i\mathbf{k} \cdot (\mathbf{R}_m - \mathbf{R}_0)], \quad (\text{A1})$$

$$\mathcal{K}_{i,j}(\mathbf{q}) = \frac{1}{\sqrt{m_i m_j}} \sum_m K_{i,j}(m, 0) \exp[-i\mathbf{q} \cdot (\mathbf{R}_m - \mathbf{R}_0)], \quad (\text{A2})$$

where S_i and m_i are the magnitude of the atomic spin and the relative atomic mass of the i th atom, respectively. \mathbf{R}_m is the position vector of the m th unit cell. $X_{i,j}$ and $K_{i,j}$ are the ECCs and the 2nd-IFCs between atoms (or vibrational degree of freedom) i and j . \mathbf{k} and \mathbf{q} are the magnon's and phonon's wave vectors that traverse the whole Brillouin zone instead of only the yz plane. It should be noted that, by multiplying the factor $\sqrt{S_i S_j}$, the ECCs adopted here exactly correspond to that given by the Liechtenstein method. The diagonalization of dynamical matrices defined in Eqs. (A1) and (A2) will yield the phonon's and magnon's dispersion relations shown in Fig. 2.

Unlike the form defined in Ref. [64], the magnon-phonon scattering amplitude here needs to be rewritten in the modal space as

$$\begin{aligned} \mathbb{M}_{\gamma,\gamma',\lambda}(\mathbf{k}, \mathbf{q}) = & \sum_{m,n} \sum_{i,j,k} \frac{\hbar}{\sqrt{2\omega_{\mathbf{q},\lambda} N m_k}} M_{i,j,k}(m, n, 0) \\ & \times \varphi_{-\mathbf{k},\gamma,i} \varphi_{\mathbf{k}-\mathbf{q},\gamma',j} \phi_{\mathbf{q},\lambda,k} \\ & \times \exp[-i\mathbf{k} \cdot (\mathbf{R}_m - \mathbf{R}_0)] \\ & \times \exp[i(\mathbf{k} - \mathbf{q}) \cdot (\mathbf{R}_n - \mathbf{R}_0)], \end{aligned} \quad (\text{A3})$$

where \hbar and N is the Planck constant and the sampling number of wave vectors \mathbf{k} and \mathbf{q} . $\omega_{\mathbf{q},\lambda}$ is the energy of the phonon with wave vector \mathbf{q} at branch λ . $\varphi_{\mathbf{k},\gamma}$ and $\phi_{\mathbf{q},\lambda}$ are the eigenvectors of magnons and phonons at specific modes, respectively. $M_{i,j,k}$ is the linear expansion coefficient of the exchange-coupling constant between atoms i and j to the vibrational degree of freedom k , namely the EFCs, and can be computed using the below finite displacement idea:

$$M_{i,j,k}(m, n, l) = \frac{X_{i,j}(m, n)|_{r_k^0+\delta} - X_{i,j}(m, n)|_{r_k^0-\delta}}{2\delta}, \quad (\text{A4})$$

where r_k^0 is the equilibrium position of the atom with the vibrational degree of freedom k . δ is a finite displacement along the direction of k .

As for the three-phonon scattering amplitude, it was already given in previous studies about anharmonic phonon transport [78,83]. Here we reproduce it using the symbols defined in this paper as

$$\begin{aligned} \mathbb{V}_{\lambda,\lambda',\lambda''}(\mathbf{q}, \mathbf{q}') &= \sum_{m,n} \sum_{i,j,k} \frac{\hbar^3}{\sqrt{8Nm_i m_j m_k}} V_{i,j,k}(m, n, 0) \\ &\times \phi_{-\mathbf{q},\lambda,i} \phi_{\mathbf{q}-\mathbf{q}',\lambda',j} \phi_{\mathbf{q}',\lambda'',k} \\ &\times \exp[-i\mathbf{q} \cdot (\mathbf{R}_m - \mathbf{R}_0)] \\ &\times \exp[i(\mathbf{q} - \mathbf{q}') \cdot (\mathbf{R}_n - \mathbf{R}_0)], \quad (\text{A5}) \end{aligned}$$

where $V_{i,j,k}$ denotes the 3rd-IFCs. In terms of the three-phonon scattering amplitude, the corresponding three-phonon scattering rates have the forms

$$\begin{aligned} \Gamma_{\lambda,\lambda',\lambda''}^{p,\pm}(\mathbf{q}, \mathbf{q}') &= \frac{3 \pm 1}{2} \frac{\pi}{\hbar} \frac{|\mathbb{V}_{\lambda,\lambda',\lambda''}(\mathbf{q}, \mathbf{q}')|^2}{\omega_{\mathbf{q},\lambda} \omega_{\mathbf{q}' \mp \mathbf{q},\lambda'} \omega_{\pm \mathbf{q}',\lambda''}} \\ &\times \delta(\omega_{\mathbf{q},\lambda} \pm \omega_{\mathbf{q}' \mp \mathbf{q},\lambda'} - \omega_{\pm \mathbf{q}',\lambda''}) \\ &\times \left(\bar{n}_{\mathbf{q}' \mp \mathbf{q},\lambda'} \mp \bar{n}_{\pm \mathbf{q}',\lambda''} + \frac{1}{2} \mp \frac{1}{2} \right), \quad (\text{A6}) \end{aligned}$$

where “+” and “−” denote the absorption and emission processes of three-phonon scattering, respectively.

Besides, the expression of phonon-isotope scattering rate has been given in previous studies [119,120]. We also reproduce it here for reference as follows:

$$\begin{aligned} \Gamma_{\lambda,\lambda'}^p(\mathbf{q}, \mathbf{q}') &= \frac{\pi \omega_{\mathbf{q},\lambda} \omega_{\mathbf{q}',\lambda'}}{2N\hbar} \delta(\omega_{\mathbf{q},\lambda} - \omega_{\mathbf{q}',\lambda'}) \\ &\times \sum_i g_i |\vec{\phi}_{\mathbf{q}',\lambda';i}^* \cdot \vec{\phi}_{\mathbf{q},\lambda;i}|^2, \quad (\text{A7}) \end{aligned}$$

where $g_i = \sum_{\alpha} f_i^{\alpha} (1 - m_i^{\alpha} / \bar{m}_i)^2$ is the Pearson deviation coefficient of masses m_i^{α} of isotopes α of atom i . f_i^{α} and $\bar{m}_i = m_i$ are the amount ratio of isotope α and the average mass of atom i , respectively. For iron atoms, $g_i = 8.219 \times 10^{-5}$ is used in this work.

APPENDIX B: CONVERGENCE TEST OF K-MESH

We show the convergence testing results in this section. To find a sufficiently dense grid to obtain reasonable thermal conductivities, as shown in Fig. 8, we computed the exact thermal conductivities of magnon and phonon using various k meshes, i.e., $N \times N \times N$ ($N = 12, 14, \dots, 30$), at temperatures of 10, 100, 300, and 1000 K. It is seen that thermal conductivities converge harder at low temperatures. However, a k mesh of $28 \times 28 \times 28$ is dense enough for thermal conductivities to converge over temperatures from 10 K to 1000 K. A denser k mesh may yield more accurate results at low temperatures but provide no more information except for wasting more computing resources.

In particular, we emphasize that the poor convergence at 10 K does not affect our conclusions about possible hydrodynamic transport in Sec. III E. To demonstrate this point, we extend the grid point number to the largest that we can use,

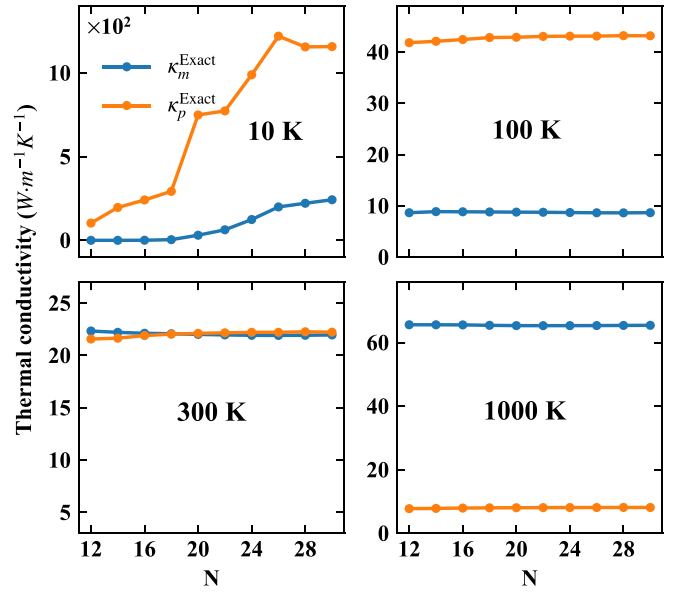


FIG. 8. Magnon's (dotted blue lines, κ_m^{Exact}) and phonon's (dotted orange lines, κ_p^{Exact}) exact thermal conductivities calculated with various k meshes, i.e., $N \times N \times N$ ($N = 12, 14, \dots, 30$), at different temperatures of 10, 100, 300, and 1000 K. No boundary scattering was considered in these calculations.

i.e., $N = 34$, and perform the convergence test. The results are shown in Fig. 9. We would like to explain the validity of our conclusion from two aspects below.

On the one hand, it can be seen that thermal conductivities have an increasing trend or oscillatory behavior with the increase of N , and these unstable values become stable as temperature increases. We may not be able to conclude

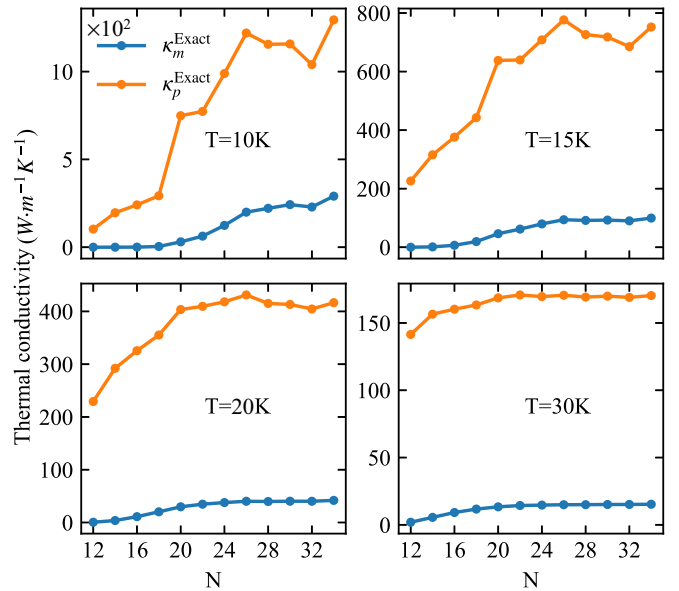


FIG. 9. Magnon's (dotted blue lines, κ_m^{Exact}) and phonon's (dotted orange lines, κ_p^{Exact}) exact thermal conductivities calculated with various k meshes, i.e., $N \times N \times N$ ($N = 12, 14, \dots, 34$), at different temperatures of 10, 15, 20, and 30 K. No boundary scattering was considered in these calculations.

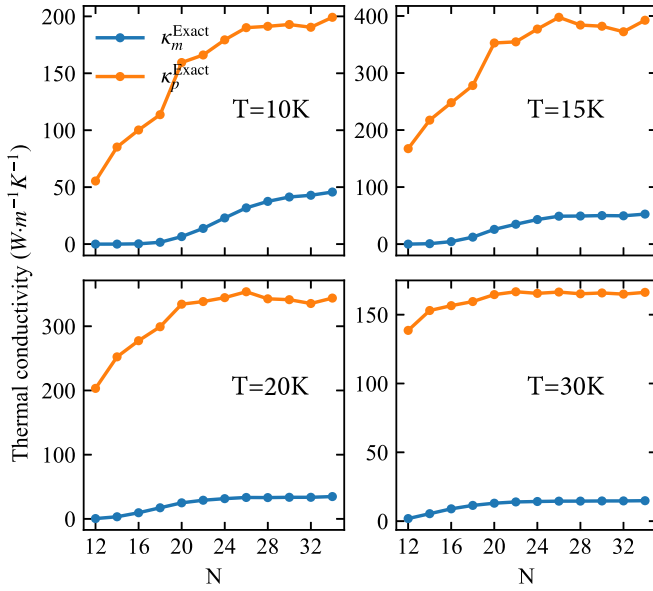


FIG. 10. Magnon's (dotted blue lines, κ_m^{Exact}) and phonon's (dotted orange lines, κ_p^{Exact}) exact thermal conductivities calculated with various k meshes, i.e., $N \times N \times N$ ($N = 12, 14, \dots, 34$), at different temperatures of 10, 15, 20, and 30 K. The Casimir length of 100 μm was considered in these calculations.

that the thermal conductivities are convergent at 10 K, but we can think that they are nearly convergent above 15 K (in fact, at 15 K, they look oscillatory as N increases). That is, thermal conductivities and other thermal properties we calculated at 15 K should be relatively convergent. Meanwhile, we emphasize that the *exact* propagation length (bold solid lines in Fig. 7), i.e., the effective collective mean free path of a group of particles (magnons, phonons, or all particles), is bound to increase as the temperature decreases. So, at temperatures below 15 K, the *exact* propagation lengths should be greater than that above 15 K, i.e., near or greater than 100 μm , which means the hydrodynamic transport may still occur.

On the other hand, as the grid becomes denser, the exact thermal conductivities (at 10 and 15 K) show rising trends overall, which implies the ideal thermal conductivities (with a dense-enough grid) should be near or greater than that with $N = 28$. And therefore, the corresponding *exact* propagation lengths with a dense-enough grid should be greater than the current *exact* propagation lengths (see bold solid lines in Fig. 7), which will lead to a more apparent hydrodynamic behavior in the currently given temperature region (10–14 K). From this perspective, the present results even estimate the hydrodynamic behavior conservatively.

According to the above analyses, the poor convergence at low temperatures does not change the conclusion that the hydrodynamic behavior may occur at the present temperature region, i.e., 10–14 K. The current numerical results at low temperatures show at least the correct trend.

As a reference, we also show the convergence test results of thermal conductivities with the boundary scattering of 100 μm in Fig. 10 because the thermal conductivities in Fig. 3 were given under this condition. A more stable convergence can be

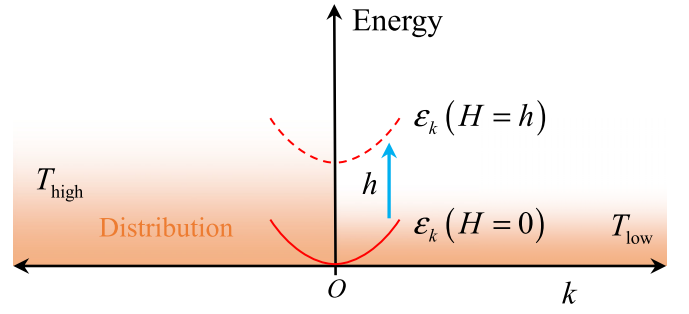


FIG. 11. Schematic of the mechanism of external magnetic field suppressing magnon's transport.

obtained after considering the boundary scattering, indicating results in Fig. 3 should be credible under the MP-BTE method in the present work.

APPENDIX C: HIGH-FIELD-SUPPRESSED MAGNON TRANSPORT

In this section, we briefly analyze how strong magnetic fields suppress the magnon's transport and extract the magnon's contribution from the total thermal conductivity.

Magnon dispersion at an easy-axis magnetic field can be expressed as

$$\varepsilon_k(B) = \varepsilon_k^0 + g\mu_B B S, \quad (\text{C1})$$

where $g = 2$ is the Landé g factor of the electron, μ_B is the Bohr magneton, and B is the magnetic induction. The first term of the right-hand side of the above equation, i.e., ε_k^0 , denotes the zero-field magnon dispersion. For bcc iron, the magnon dispersion as shown in Fig. 2 is just the zero-field one. The second term is the so-called Zeeman energy, replaced by H in the main text. Therefore, the external field can raise the magnon's energy spectrum. Figure 11 shows the schematic for this process.

Besides, notice that the magnon excitation follows the Bose-Einstein distribution. At low temperatures (see the right-hand side of Fig. 11), only low-energy magnons are excited, while the high-energy magnons have negligible occupancies. So, suppose a strong-enough magnetic field is applied to increase magnons' energies so that nearly no magnon can be excited. In that case, magnons will hardly contribute to thermal transport, and the total thermal conductivity will be considered donated purely by phonons. In other words, the difference between the thermal conductivities with and without the external field can be approximately attributed to the magnon's thermal transport, i.e.,

$$\kappa_m \approx \kappa_{\text{total}}(H=0) - \kappa_{\text{total}}(H \rightarrow +\infty), \quad (\text{C2})$$

since phonons are considered unaffected by the external field. This idea has been widely adopted in thermal measurements of magnetic materials as a prob to detect the quantum transport behavior of spin or magnon [104,105].

However, the above approximation is valid only if the magnons are wholly frozen by the external field, which requires low-enough temperatures or strong-enough magnetic

fields. For example, $T = 10$ K and $H = 100$ meV are required in the bcc iron. At high temperatures (see the left-hand side of Fig. 11), the original magnetic field cannot freeze all magnons. And the magnons with relatively low energies still have a palpable occupancy and therefore donate to the total thermal conductivity. In this case, one will underestimate the magnon's contribution to the total thermal conductivity if using Eq. (C2).

APPENDIX D: QUALITATIVE RELATIONSHIP BETWEEN CURIE POINT AND TRANSITION TEMPERATURE

We provide a brief qualitative analysis of the relationship between the Curie temperature (T_C) and the magnon's thermal conductivity transition temperature (T_M , i.e., the corresponding temperature of maximum thermal conductivity) in ferromagnetic crystals.

Considering the nearest exchange interaction, the Curie temperature of a periodic ferromagnetic system can be

approximately determined as [99]

$$T_C = \frac{2}{3k_B} ZJ, \quad (\text{D1})$$

where k_B is the Boltzmann constant, Z is the coordination number ($Z = 8$ for bcc iron), and J is the effective nearest exchange-coupling constant (with energy units). On the other hand, the maximum energy of magnon is dependent on J as $\varepsilon_{\max} = 2ZJ$. So the Debye temperature (Θ) should be proportional to J , i.e., $\Theta \propto J$. Moreover, the transition temperature is usually positively correlated to the Debye temperature, i.e., $T_M \propto \Theta$. Accordingly, we can approximately consider that $T_M \propto T_C$.

Note that the above qualitative analysis has adopted many rough assumptions and approximations. Therefore, the final relation may not always be proper, especially for different materials with different crystal symmetries. Besides, the specific scattering detail is also essential to determine T_M . But we can broadly consider that ferromagnetic materials with higher T_C may typically also have higher T_M .

-
- [1] I. Žutić, J. Fabian, and S. Das Sarma, *Rev. Mod. Phys.* **76**, 323 (2004).
 - [2] A. Hoffmann and S. D. Bader, *Phys. Rev. Appl.* **4**, 047001 (2015).
 - [3] G. E. W. Bauer, E. Saitoh, and B. J. van Wees, *Nat. Mater.* **11**, 391 (2012).
 - [4] S. R. Boona, R. C. Myers, and J. P. Heremans, *Energy Environ. Sci.* **7**, 885 (2014).
 - [5] K.-i. Uchida, *Proc. Jpn. Acad. Ser. B* **97**, 69 (2021).
 - [6] L. Zhang, J. Ren, J.-S. Wang, and B. Li, *Phys. Rev. Lett.* **105**, 225901 (2010).
 - [7] T. Ideue, T. Kurumaji, S. Ishiwata, and Y. Tokura, *Nat. Mater.* **16**, 797 (2017).
 - [8] Y. H. Gao and G. Chen, *SciPost Phys. Core* **2**, 004 (2020).
 - [9] K. Uchida, H. Adachi, T. An, T. Ota, M. Toda, B. Hillebrands, S. Maekawa, and E. Saitoh, *Nat. Mater.* **10**, 737 (2011).
 - [10] J. Flipse, F. K. Dejene, D. Wagenaar, G. E. W. Bauer, J. Ben Youssef, and B. J. van Wees, *Phys. Rev. Lett.* **113**, 027601 (2014).
 - [11] V. Franco, J. Blázquez, J. Ipus, J. Law, L. Moreno-Ramírez, and A. Conde, *Prog. Mater. Sci.* **93**, 112 (2018).
 - [12] A. J. Minnich, M. S. Dresselhaus, Z. F. Ren, and G. Chen, *Energy Environ. Sci.* **2**, 466 (2009).
 - [13] M. Zebarjadi, K. Esfarjani, M. S. Dresselhaus, Z. F. Ren, and G. Chen, *Energy Environ. Sci.* **5**, 5147 (2012).
 - [14] F.-H. Sun, S. Ma, W. Zhao, C. Li, X. Sang, P. Wei, and Q. Zhang, *Rep. Prog. Phys.* **84**, 096501 (2021).
 - [15] L. Wang and B. Li, *Phys. Rev. Lett.* **99**, 177208 (2007).
 - [16] Y. Li, X. Shen, Z. Wu, J. Huang, Y. Chen, Y. Ni, and J. Huang, *Phys. Rev. Lett.* **115**, 195503 (2015).
 - [17] X.-F. Peng, K.-Q. Chen, Q. Wan, B. S. Zou, and W. Duan, *Phys. Rev. B* **81**, 195317 (2010).
 - [18] N. Li, J. Ren, L. Wang, G. Zhang, P. Hänggi, and B. Li, *Rev. Mod. Phys.* **84**, 1045 (2012).
 - [19] X. Gu, Y. Wei, X. Yin, B. Li, and R. Yang, *Rev. Mod. Phys.* **90**, 041002 (2018).
 - [20] J. Chen, X. Xu, J. Zhou, and B. Li, *Rev. Mod. Phys.* **94**, 025002 (2022).
 - [21] M. Yamashita, N. Nakata, Y. Kasahara, T. Sasaki, N. Yoneyama, N. Kobayashi, S. Fujimoto, T. Shibauchi, and Y. Matsuda, *Nat. Phys.* **5**, 44 (2009).
 - [22] M. Yamashita, N. Nakata, Y. Senshu, M. Nagata, H. M. Yamamoto, R. Kato, T. Shibauchi, and Y. Matsuda, *Science* **328**, 1246 (2010).
 - [23] S. Y. Li, L. Taillefer, C. H. Wang, and X. H. Chen, *Phys. Rev. Lett.* **95**, 156603 (2005).
 - [24] C. S. Lue, C. N. Kuo, D. S. Tasi, Y. K. Kuo, Z. He, and M. Itoh, *Phys. Rev. B* **78**, 012406 (2008).
 - [25] M. Montagnese, M. Otter, X. Zotos, D. A. Fishman, N. Hlubek, O. Mityashkin, C. Hess, R. Saint-Martin, S. Singh, A. Revcolevschi, and P. H. M. van Loosdrecht, *Phys. Rev. Lett.* **110**, 147206 (2013).
 - [26] M. Gillig, X. Hong, P. Sakrikar, G. Bastien, A. U. B. Wolter, L. Heinze, S. Nishimoto, B. Büchner, and C. Hess, *Phys. Rev. B* **104**, 235129 (2021).
 - [27] S. R. Boona and J. P. Heremans, *Phys. Rev. B* **90**, 064421 (2014).
 - [28] J. S. Jamison, Z. Yang, B. L. Giles, J. T. Brangham, G. Wu, P. C. Hammel, F. Yang, and R. C. Myers, *Phys. Rev. B* **100**, 134402 (2019).
 - [29] K. Wang, X. Xu, Y. Cheng, M. Zhang, J.-S. Wang, H. Wang, and G. Zhang, *Appl. Phys. Lett.* **118**, 023102 (2021).
 - [30] J.-S. Wang, J. Wang, and N. Zeng, *Phys. Rev. B* **74**, 033408 (2006).
 - [31] N. Mingo, *Phys. Rev. B* **74**, 125402 (2006).
 - [32] Y. Xu, J.-S. Wang, W. Duan, B.-L. Gu, and B. Li, *Phys. Rev. B* **78**, 224303 (2008).
 - [33] M. Luisier, *Phys. Rev. B* **86**, 245407 (2012).

- [34] Y. Lee, M. Bescond, D. Logoteta, N. Cavassilas, M. Lannoo, and M. Luisier, *Phys. Rev. B* **97**, 205447 (2018).
- [35] J. Dai and Z. Tian, *Phys. Rev. B* **101**, 041301(R) (2020).
- [36] Y. Guo, M. Bescond, Z. Zhang, M. Luisier, M. Nomura, and S. Volz, *Phys. Rev. B* **102**, 195412 (2020).
- [37] A. Pecchia, A. D. Carlo, A. Gagliardi, S. Sanna, T. Frauenheim, and R. Gutierrez, *Nano Lett.* **4**, 2109 (2004).
- [38] N. Sergueev, D. Roubtsov, and H. Guo, *Phys. Rev. Lett.* **95**, 146803 (2005).
- [39] M. Paulsson, T. Frederiksen, and M. Brandbyge, *Phys. Rev. B* **72**, 201101(R) (2005).
- [40] J.-T. Lü, R. B. Christensen, G. Foti, T. Frederiksen, T. Gunst, and M. Brandbyge, *Phys. Rev. B* **89**, 081405(R) (2014).
- [41] D. A. Broido, A. Ward, and N. Mingo, *Phys. Rev. B* **72**, 014308 (2005).
- [42] W. Li, N. Mingo, L. Lindsay, D. A. Broido, D. A. Stewart, and N. A. Katcho, *Phys. Rev. B* **85**, 195436 (2012).
- [43] G. Fugallo, M. Lazzeri, L. Paulatto, and F. Mauri, *Phys. Rev. B* **88**, 045430 (2013).
- [44] L. Chaput, *Phys. Rev. Lett.* **110**, 265506 (2013).
- [45] T. Feng and X. Ruan, *Phys. Rev. B* **97**, 045202 (2018).
- [46] T. Gunst, T. Markussen, K. Stokbro, and M. Brandbyge, *Phys. Rev. B* **93**, 035414 (2016).
- [47] J. Zhou, B. Liao, and G. Chen, *Semicond. Sci. Technol.* **31**, 043001 (2016).
- [48] M. Fiorentini and N. Bonini, *Phys. Rev. B* **94**, 085204 (2016).
- [49] C. Li, N. K. Ravichandran, L. Lindsay, and D. Broido, *Phys. Rev. Lett.* **121**, 175901 (2018).
- [50] A. Kundu, X. Yang, J. Ma, T. Feng, J. Carrete, X. Ruan, G. K. H. Madsen, and W. Li, *Phys. Rev. Lett.* **126**, 115901 (2021).
- [51] X. Zhang, S. Li, A. Wang, and H. Bao, *Phys. Rev. B* **106**, 094313 (2022).
- [52] Z. Fan, Luiz Felipe C. Pereira, H.-Q. Wang, J.-C. Zheng, D. Donadio, and A. Harju, *Phys. Rev. B* **92**, 094301 (2015).
- [53] Y. Zhou and M. Hu, *Phys. Rev. B* **95**, 115313 (2017).
- [54] X.-K. Chen, J. Liu, Z.-H. Peng, D. Du, and K.-Q. Chen, *Appl. Phys. Lett.* **110**, 091907 (2017).
- [55] T. Feng, Y. Zhong, J. Shi, and X. Ruan, *Phys. Rev. B* **99**, 045301 (2019).
- [56] T. M. Gibbons and S. K. Estreicher, *Phys. Rev. Lett.* **102**, 255502 (2009).
- [57] J. Kang and L.-W. Wang, *Phys. Rev. B* **96**, 020302(R) (2017).
- [58] M. Puligheddu, F. Gygi, and G. Galli, *Phys. Rev. Mater.* **1**, 060802(R) (2017).
- [59] H. Pan, Z.-K. Ding, Y.-J. Zeng, Q.-Q. Li, L.-M. Tang, and K.-Q. Chen, *Europhys. Lett.* **138**, 36001 (2022).
- [60] L. Zhang, J.-S. Wang, and B. Li, *Phys. Rev. B* **81**, 100301(R) (2010).
- [61] J. Ren and J.-X. Zhu, *Phys. Rev. B* **88**, 094427 (2013).
- [62] J. Ren, J. Fransson, and J.-X. Zhu, *Phys. Rev. B* **89**, 214407 (2014).
- [63] Z.-Q. Zhang and J.-T. Lü, *Phys. Rev. B* **96**, 125432 (2017).
- [64] H. Pan, L.-M. Tang, and K.-Q. Chen, *Phys. Rev. B* **105**, 064401 (2022).
- [65] P.-W. Ma, S. L. Dudarev, and C. H. Woo, *Phys. Rev. B* **85**, 184301 (2012).
- [66] J. Tranchida, S. Plimpton, P. Thibaudau, and A. Thompson, *J. Comput. Phys.* **372**, 406 (2018).
- [67] J. Hellsvik, D. Thonig, K. Modin, D. Iuşan, A. Bergman, O. Eriksson, L. Bergqvist, and A. Delin, *Phys. Rev. B* **99**, 104302 (2019).
- [68] X. Wu, Z. Liu, and T. Luo, *J. Appl. Phys.* **123**, 085109 (2018).
- [69] Y. Zhou, J. Tranchida, Y. Ge, J. Murthy, and T. S. Fisher, *Phys. Rev. B* **101**, 224303 (2020).
- [70] Y. Ge, Y. Zhou, and T. S. Fisher, *J. Appl. Phys.* **130**, 235108 (2021).
- [71] B. Flebus, K. Shen, T. Kikkawa, K.-i. Uchida, Z. Qiu, E. Saitoh, R. A. Duine, and G. E. W. Bauer, *Phys. Rev. B* **95**, 144420 (2017).
- [72] R. Schmidt and P. W. Brouwer, *Phys. Rev. B* **103**, 014412 (2021).
- [73] B. Liao, J. Zhou, and G. Chen, *Phys. Rev. Lett.* **113**, 025902 (2014).
- [74] A. I. Bezuglyj, V. A. Shklovskij, V. V. Kruglyak, and R. V. Vovk, *Phys. Rev. B* **100**, 214409 (2019).
- [75] S. Streib, N. Vidal-Silva, K. Shen, and G. E. W. Bauer, *Phys. Rev. B* **99**, 184442 (2019).
- [76] R. Peierls, *Ann. Phys.* **395**, 1055 (1929).
- [77] J. M. Ziman, *Electrons and Phonons: The Theory of Transport Phenomena in Solids* (Clarendon Press, Oxford, 1960).
- [78] W. Li, J. Carrete, N. A. Katcho, and N. Mingo, *Comput. Phys. Commun.* **185**, 1747 (2014).
- [79] F. Giustino, M. L. Cohen, and S. G. Louie, *Phys. Rev. B* **76**, 165108 (2007).
- [80] G. P. Srivastava, *The Physics of Phonons* (Routledge, London, 1990).
- [81] A. Sparavigna, *Phys. Rev. B* **65**, 064305 (2002).
- [82] D. A. Broido, L. Lindsay, and A. Ward, *Phys. Rev. B* **86**, 115203 (2012).
- [83] J. Carrete, B. Vermeersch, A. Katre, A. van Roekeghem, T. Wang, G. K. Madsen, and N. Mingo, *Comput. Phys. Commun.* **220**, 351 (2017).
- [84] M. Omini and A. Sparavigna, *Phys. B: Condens. Matter* **212**, 101 (1995).
- [85] V. J. Minkiewicz, G. Shirane, and R. Nathans, *Phys. Rev.* **162**, 528 (1967).
- [86] J. W. Lynn, *Phys. Rev. B* **11**, 2624 (1975).
- [87] G. Kresse and J. Furthmüller, *Phys. Rev. B* **54**, 11169 (1996).
- [88] G. Kresse and J. Furthmüller, *Comput. Mater. Sci.* **6**, 15 (1996).
- [89] P. E. Blöchl, *Phys. Rev. B* **50**, 17953 (1994).
- [90] G. Kresse and D. Joubert, *Phys. Rev. B* **59**, 1758 (1999).
- [91] J. P. Perdew, K. Burke, and M. Ernzerhof, *Phys. Rev. Lett.* **77**, 3865 (1996).
- [92] A. Togo and I. Tanaka, *Scr. Mater.* **108**, 1 (2015).
- [93] Z.-K. Ding, Y.-J. Zeng, H. Pan, N. Luo, J. Zeng, L.-M. Tang, and K.-Q. Chen, *Phys. Rev. B* **106**, L121401 (2022).
- [94] T. Ozaki, *Phys. Rev. B* **67**, 155108 (2003).
- [95] T. Ozaki and H. Kino, *Phys. Rev. B* **72**, 045121 (2005).
- [96] A. Liechtenstein, M. Katsnelson, V. Antropov, and V. Gubanov, *J. Magn. Magn. Mater.* **67**, 65 (1987).
- [97] M. I. Katsnelson and A. I. Liechtenstein, *Phys. Rev. B* **61**, 8906 (2000).
- [98] M. Y. Lavrentiev, D. Nguyen-Manh, and S. L. Dudarev, *Phys. Rev. B* **81**, 184202 (2010).
- [99] A. Terasawa, M. Matsumoto, T. Ozaki, and Y. Gohda, *J. Phys. Soc. Jpn.* **88**, 114706 (2019).
- [100] N. G. Bäklund, *J. Phys. Chem. Solids* **20**, 1 (1961).

- [101] R. W. Powell, *Proc. Phys. Soc.* **51**, 407 (1939).
- [102] F. Körmann, B. Grabowski, B. Dutta, T. Hickel, L. Mauger, B. Fultz, and J. Neugebauer, *Phys. Rev. Lett.* **113**, 165503 (2014).
- [103] P. Buczek, A. Ernst, and L. M. Sandratskii, *Phys. Rev. Lett.* **106**, 157204 (2011).
- [104] B. C. Sales, M. D. Lumsden, S. E. Nagler, D. Mandrus, and R. Jin, *Phys. Rev. Lett.* **88**, 095901 (2002).
- [105] R. Jin, Y. Onose, Y. Tokura, D. Mandrus, P. Dai, and B. C. Sales, *Phys. Rev. Lett.* **91**, 146601 (2003).
- [106] S. M. Rezende and J. C. López Ortiz, *Phys. Rev. B* **91**, 104416 (2015).
- [107] G. Chen, *Nat. Rev. Phys.* **3**, 555 (2021).
- [108] M. Markov, J. Sjakste, G. Barbarino, G. Fugallo, L. Paulatto, M. Lazzeri, F. Mauri, and N. Vast, *Phys. Rev. Lett.* **120**, 075901 (2018).
- [109] R. A. Guyer and J. A. Krumhansl, *Phys. Rev.* **148**, 778 (1966).
- [110] Z. Ding, K. Chen, B. Song, J. Shin, A. A. Maznev, K. A. Nelson, and G. Chen, *Nat. Commun.* **13**, 285 (2022).
- [111] G. Qin, H. Wang, L. Zhang, Z. Qin, and M. Hu, *J. Mater. Chem. C* **8**, 3520 (2020).
- [112] Q.-Q. Li, S. Li, D. Wu, Z.-K. Ding, X.-H. Cao, L. Huang, H. Pan, B. Li, K.-Q. Chen, and X.-D. Duan, *Appl. Phys. Lett.* **119**, 162402 (2021).
- [113] Y.-J. Zeng, Y.-X. Feng, L.-M. Tang, and K.-Q. Chen, *Appl. Phys. Lett.* **118**, 183103 (2021).
- [114] Q. Liu, J. J. Li, D. Wu, X. Q. Deng, Z. H. Zhang, Z. Q. Fan, and K.-Q. Chen, *Phys. Rev. B* **104**, 045412 (2021).
- [115] C.-W. Wu, X. Ren, G. Xie, W.-X. Zhou, G. Zhang, and K.-Q. Chen, *Phys. Rev. Appl.* **18**, 014053 (2022).
- [116] P.-Z. Jia, J.-P. Xie, X.-K. Chen, Y. Zhang, X. Yu, Y.-J. Zeng, Z.-X. Xie, Y.-X. Deng, and W.-X. Zhou, *J. Phys.: Condens. Matter* **35**, 073001 (2023).
- [117] R. Bosisio, S. Valentini, F. Mazza, G. Benenti, R. Fazio, V. Giovannetti, and F. Taddei, *Phys. Rev. B* **91**, 205420 (2015).
- [118] X. Zhao, J. C. Wu, Z. Y. Zhao, Z. Z. He, J. D. Song, J. Y. Zhao, X. G. Liu, X. F. Sun, and X. G. Li, *Appl. Phys. Lett.* **108**, 242405 (2016).
- [119] S.-i. Tamura, *Phys. Rev. B* **27**, 858 (1983).
- [120] A. Kundu, N. Mingo, D. A. Broido, and D. A. Stewart, *Phys. Rev. B* **84**, 125426 (2011).